Dartmouth College

# Dartmouth Digital Commons

Open Dartmouth: Published works by Dartmouth faculty

Faculty Work

9-20-2004

# Kinematics of X-Ray–Emitting Components in Cassiopeia A

Tracey DeLaney
*University of Minnesota*

Lawrence Rudnick
*University of Minnesota*

Robert A. Fesen
*Dartmouth College*

T. W. Jones
*University of Minnesota*

Follow this and additional works at: https://digitalcommons.dartmouth.edu/facoa

Part of the Stars, Interstellar Medium and the Galaxy Commons

# KINEMATICS OF X-RAY–EMITTING COMPONENTS IN CASSIOPEIA A

Tracey DeLaney,[1] Lawrence Rudnick,[1] Robert A. Fesen,[2] T. W. Jones,[1] Robert Petre,[3] and Jon A. Morse[4]

## ABSTRACT

We present high-resolution X-ray proper-motion measurements of Cassiopeia A using *Chandra X-Ray Observatory* observations from 2000 and 2002. We separate the emission into four spectrally distinct classes: Si-dominated, Fe-dominated, low-energy–enhanced, and continuum-dominated. These classes also represent distinct spatial and kinematic components. The Si- and Fe-dominated classes are ejecta and have a mean expansion rate of 0.2% $yr^{-1}$. This is the same as for the forward shock filaments but less than the 0.3% $yr^{-1}$ characteristic of optical ejecta. The low-energy–enhanced spectral class possibly illuminates a clumpy circumstellar component and has a mean expansion rate of 0.05% $yr^{-1}$. The continuum-dominated emission likely represents the forward shock and consists of diffuse circumstellar material, which is seen as a circular ring around the periphery of the remnant as well as projected across the center.

*Subject headings:* ISM: individual (Cassiopeia A) — supernova remnants

*On-line material:* machine-readable table

## 1. INTRODUCTION

Cassiopeia A (Cas A) is the youngest known ($\sim$330 yr; Thorstensen et al. 2001) Galactic supernova remnant (SNR). It is about 3.4 kpc (Reed et al. 1995) away and was most likely the result of either a Type Ib or IIn supernova explosion (Chevalier & Oishi 2003). As one of the brightest X-ray and radio sources in the sky, Cas A is one of the best targets for studying SNR evolution. At radio, X-ray, and optical wavelengths, Cas A is dominated by a 3$\farcm$5 diameter bright ring of emission with a fainter 5$'$ diameter plateau of radio and X-ray emission. The X-ray emission is dominated by a thermal spectrum rich in emission lines from highly ionized atoms. The radio emission is consistent with synchrotron radiation from relativistic electrons accelerated at shocks. The optical emission originates from a complex system of chemically enriched knots.

The kinematics of small- and large-scale radio features of Cas A are well studied. The small-scale radio knots are significantly decelerated relative to the X-ray and optical emission. They are not in homologous expansion, and there are even inward-moving knots. The expansion rates of the small-scale features of the bright ring vary by over a factor of 2 as a function of azimuth with a mean rate of 0.11% $yr^{-1}$ (Anderson & Rudnick 1995; Koralesky et al. 1998; Tuffs 1986). The bulk expansion of Cas A has been measured in several ways by Anderson & Rudnick (1995), Agüeros & Green (1999), and DeLaney & Rudnick (2003), with reported expansion rates of $\approx$0.11, $\approx$0.22, and $\approx$0.07 percent $yr^{-1}$, respectively. For this discussion, we adopt the DeLaney & Rudnick (2003) value of 0.07% $yr^{-1}$ because it is the least contaminated by brightness changes and azimuthal asymmetries.

The optical components of Cas A consist of slow-moving ($\lesssim$500 km s$^{-1}$) quasi-stationary flocculi (QSFs) and fast-moving knots (FMKs; 4000–6000 km s$^{-1}$, $\approx$0.3% $yr^{-1}$) (Kamper & van den Bergh 1976; van den Bergh & Kamper 1985). The QSFs are thought to be shocked circumstellar material (CSM) from the presupernova wind of the progenitor, while most of the FMKs are located on the bright ring and represent emission from ejecta that have interacted with the reverse shock. There are also outlying knots of enriched composition with velocities from 8000 to 15,000 km s$^{-1}$ ($\approx$0.3% $yr^{-1}$; Fesen 2001).

Previous X-ray proper-motion measurements, conducted with *Einstein* and *ROSAT* at a resolution of 5$''$, showed that the mean expansion rate was 0.2% $yr^{-1}$ (Koralesky et al. 1998; Vink et al. 1998). This established a paradoxical difference in expansion rates for the cospatial bright ring measured in optical, X-ray, and radio of approximately 3 : 2 : 1, respectively (Thorstensen et al. 2001 and references therein). The factor of 2 discrepancy between the X-ray and radio expansion is a common theme in young SNRs and has been found in both Kepler's SNR (Hughes 1999; Dickel et al. 1988) and Tycho's SNR (Hughes 2000).

With the advent of the *Chandra X-Ray Observatory*, we are now able to measure proper motions with unprecedented spatial resolution. The results for the forward shock filaments around the outer edge of the remnant showed a mean expansion rate of 0.21% $yr^{-1}$ (DeLaney & Rudnick 2003), the same as the bright ring. In this paper we extend our proper-motion analysis to the rest of the SNR, for four spectrally distinct components. One of these components represents a new class of X-ray emission, while three components have been previously identified (Hughes et al. 2000). We interpret the proper motions based on these spectral components and propose a solution to the expansion rate paradox.

## 2. OBSERVATIONS, ANALYSIS, AND RESULTS

Cas A was observed for 50 ks with the ACIS-S3 chip on board *Chandra* on 2000 January 30–31 and 2002 February 6. For details of the observing parameters and data reduction, see Hwang et al. (2000), Gotthelf et al. (2001), and DeLaney &

[1] Department of Astronomy, University of Minnesota, 116 Church Street SE, Minneapolis, MN 55455; tdelaney@astro.umn.edu, larry@astro.umn.edu, twj@astro.umn.edu.
[2] Department of Physics and Astronomy, Dartmouth College, Hanover, NH 03755; fesen@snr.dartmouth.edu.
[3] NASA Goddard Space Flight Center, Greenbelt, MD 20771; petre@lheavx.gsfc.nasa.gov.
[4] Department of Physics and Astronomy, Arizona State University, Box 871504, Tempe, AZ 85287-1504; Jon.Morse@asu.edu.

TABLE 1
Knot and Filament Proper Motions

| Number (1) | blc$_x$ (arcsec) (2) | blc$_y$ (arcsec) (3) | trc$_x$ (arcsec) (4) | trc$_y$ (arcsec) (5) | $\mu_x$ (arcsec yr$^{-1}$) (6) | $\mu_y$ (arcsec yr$^{-1}$) (7) | $v_r$ (% yr$^{-1}$) (8) | $\delta v_r$ (% yr$^{-1}$) (9) | Class (10) |
|---|---|---|---|---|---|---|---|---|---|
| 1..................... | 2.0 | −105.3 | 8.4 | −99.9 | 0.01 | −0.20 | 0.19 | 0.07 | L |
| 2..................... | 60.5 | −122.5 | 67.4 | −115.6 | 0.05 | −0.01 | 0.03 | 0.05 | M |
| 3..................... | 25.6 | −83.6 | 32.0 | −77.2 | 0.01 | −0.03 | 0.03 | 0.09 | M |
| 4..................... | −32.0 | −65.4 | −25.1 | −58.1 | −0.01 | −0.10 | 0.15 | 0.11 | S |
| 5..................... | −7.4 | −33.0 | −1.0 | −27.1 | −0.02 | 0.05 | −0.15 | 0.24 | L |

Notes.—Table 1 is published in its entirety in the electronic edition of the *Astrophysical Journal*. A portion is shown here for guidance regarding its form and content. All knots have been assigned a constant error of 0″07 yr$^{-1}$. Col. (1): Knot or filament designation number. Cols. (2)–(5): Location of bottom left corner (blc) and top right corner (trc) of box defining the region used to measure each knot or filament and extract spectra (arcseconds of offset on epoch 2002 image with respect to the optical expansion center at R.A. = 23$^h$23$^m$27$^s$77, decl. = +58°48′49″4 (J2000.0) (Thorstensen et al. 2001). Cols. (6)–(7): Proper motion in right ascension and declination (″ yr$^{-1}$). Positive right ascension offset or motion is defined to be westward. Col. (8): Radial component of motion (% yr$^{-1}$). Col. (9): Error in radial expansion (% yr$^{-1}$). Col. (10): Spectral classification: S = Si-dominated, F = Fe-dominated, L = LowE-enhanced, C = continuum-dominated, and M = mixture of two or more classes.

Rudnick (2003). To measure proper motions, we registered the 2000 and 2002 broadband (0.3–10 keV) X-ray images by aligning them on the point source as described in DeLaney & Rudnick (2003). The uncertainty of the registration to the point source is 0″015 based on Monte Carlo simulations, which translates to a proper-motion error of 0.005% yr$^{-1}$ at the mean radius of the exterior forward shock filaments (150″). The possible 0″02 yr$^{-1}$ (Thorstensen et al. 2001) motion of the point source would result in a maximum proper-motion error of 0.013% yr$^{-1}$ at 150″. We constrained rotation between the two images by requiring the bright knots in the northeast jet to have no average rotation. The jet knots are the least decelerated features in the remnant and so should be the least affected by CSM interactions. The uncertainty in rotation alignment is less than 0°05. The proper-motion measurements for 261 knots and filaments were then made by minimizing $\chi^2$ for a ≈7″ region around each feature, using the difference maps between the 2000 image and a set of 2002 images, shifted over a range of ±2″5 in both right ascension (R.A.) and declination (decl.). DeLaney & Rudnick (2003) contains a detailed description of the one-dimensional analog of this procedure. We assigned an error of 0″07 yr$^{-1}$ to all 261 features, which corresponds to the top 20% of the Monte Carlo errors derived in DeLaney & Rudnick (2003), where the mean error was 0″04 yr$^{-1}$. These Monte Carlo simulations include problems that would arise from features of varying sizes and the different point-spread functions across the remnant, such as affects the 261 features measured here. The positions and proper motions for the 261 features are shown in Table 1. We determined the radial component of the motion for each knot or filament and calculated the radial expansion rate ($v_r$) using the distance from the optical expansion center at R.A. = 23$^h$23$^m$27$^s$77, decl. = +58°48′49″4 (J2000.0) (Thorstensen et al. 2001).

The 261 knots and filaments were spectrally classified using both extracted spectra and spectral tomography, as discussed below. Based on the extracted spectra, four major classes were identified: Si-dominated, Fe-dominated, low-energy– (LowE) enhanced, and continuum-dominated. The Si-, Fe-, and continuum-dominated classes were previously identified by Hughes et al. (2000). Representative spectra are shown in Figure 1. The Si-dominated emission is marked by very strong line emission from Si and S with contributions from O, Ca, Ar, and Mg. The Fe-dominated spectrum shows strong Fe L and Fe K emission and can in some cases be modeled with nearly pure Fe emission (Hwang & Laming 2003; Laming & Hwang 2003). The

LowE-enhanced emission shows a relative increase in emission at low energies (≈0.8–1.6 keV) compared to the global spectrum. The continuum-dominated emission is marked by very little or no line emission and an increase in 4–6 keV emission. Only 50% of the knots and filaments can be cleanly classified using their spectra alone. The remaining features combine the characteristics of two or more of the four basic classes identified above.

To separate overlapping spectral structures and to spatially visualize the spectral components, we used spectral tomography. The spectral tomography technique has been used to analyze the spectra of radio galaxies (Katz-Stone & Rudnick 1997) and supernova remnants (DeLaney et al. 2002). It involves taking differences between images from two different energies with a scale factor chosen to accentuate features of interest. In Figure 2 we show four tomography images, each representing the dominant spectral type indicated by the spectra in Figure 1. To make the tomography images, we first constructed emission-line images for Si (1.72–1.96 keV, which includes Al and possibly weak Mg), Fe L+Ne (0.9–1.15 keV, which includes Ni), and Fe L+Mg (1.35–1.55 keV) and an image of the high-energy continuum (HEC) region from 4 to 6 keV. These energy ranges were chosen to exploit the differences between the spectral classes. The images were convolved to 3″ resolution, and there was no background subtraction or correction applied for differential absorption across the remnant. The Si-dominated image was constructed by scaling and subtracting the HEC image from the Si image. Regions that are bright on the Si-dominated image represent ejecta whose emission is dominated by strong emission lines of the Si group (Si, S, Ar, and Ca), which all scale with the Si line (Hwang et al. 2000). Regions that are dark on the Si-dominated image represent features where the line emission is not dominant with respect to the continuum. The scale factor was chosen to separate the bimodal distribution of ratios in the log (Si/HEC) image. The appearance of the image in Figure 2 is only weakly dependent on the value of the scale factor. Because only the HEC image was subtracted to create the Si-dominated image, there are low levels of contamination from the Fe-dominated and LowE-enhanced classes. Subtracting out these two components does not significantly alter the Si-dominated image because the relative strength of the Si emission is very strong compared to the other classes.

The continuum-dominated image was made in the same way as the Si-dominated image, but with a slightly different scaling factor to better show the continuum-dominated component.
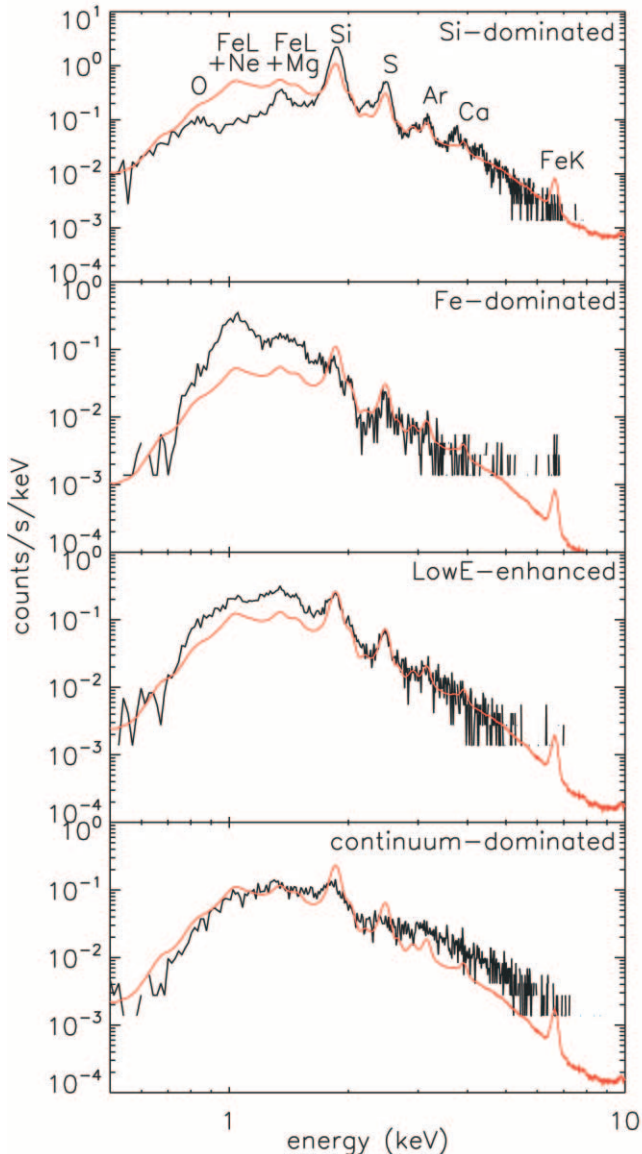
Fig. 1.—*Chandra* ACIS-S spectra of Cas A showing the global spectrum (*red*) and typical spectra for the four spectral classes identified in the text. The Si-dominated emission is marked by very strong Si group emission. The Fe-dominated spectrum shows strong Fe L and Fe K emission. The LowE-enhanced emission shows a relative increase in emission at low energies compared to the global spectrum. The continuum-dominated emission is marked by very little or no line emission and an increase in 4–6 keV emission relative to the global spectrum.

The brightness on the image was reversed so the continuum-dominated emission appears positive, while the Si-dominated emission appears negative. The Fe-dominated image was constructed from scaling and subtracting the Fe L+Mg image from the Fe L+Ne image. The bright areas represent regions where the ratio of Fe L+Ne to Fe L+Mg is greater than 1, which is unique to the Fe-dominated ejecta class. The LowE-enhanced image was made by first scaling and subtracting the Si image from the Fe L+Ne image. Because the resulting image also contained significant Fe-dominated ejecta emission, a second scaling and subtraction was applied using the positive brightness areas on the Fe-dominated image to eliminate regions with strong Fe ejecta emission. The resulting image only shows those regions with spectra similar to the LowE-enhanced spectrum in Figure 1.

The Si-dominated and Fe-dominated tomography images basically reproduce the spatial distributions of Si and Fe as shown by the equivalent width images in Hwang et al. (2000), with the exception that the western region does not show as much Si and Fe emission as is actually present because of the increased absorption of low-energy X-ray emission in that region (Koehane et al. 1996; Willingale et al. 2002). The continuum-dominated image shows the same forward shock filaments around the outer edge of the remnant as described by Gotthelf et al. (2001). There is also continuum-dominated filamentary emission interior to the bright ring of the remnant that Hughes et al. (2000) speculated results from X-ray synchrotron emission associated with the forward shock. The continuum-dominated image matches the 8–15 keV *XMM* continuum image (Bleeker et al. 2001), in the west particularly, indicating that this emission may indeed have a strong nonthermal component.

The LowE-enhanced image represents emission that has not previously been explored. Some of the LowE-enhanced emission is associated with optical QSF emission such as the features in the interior of the remnant, the bright northeast region at the outer edge of the bright ring, and the southern arc (Lawrence et al. 1995). Some of the LowE-enhanced emission has no QSF counterparts such as the emission to the southeast. This may be because the low-energy spectral region contains emission lines of O, Fe, Ne, and Mg, making it possible that some of the emission in the LowE-enhanced image is due to more than one spectral component.

The power of the tomography technique is in its ability to isolate spatially overlapping spectral components. Using spectra alone, one may misidentify features as intermediate spectral types when they are simply a combination of unrelated overlapping structures. The fact that the tomography images isolate X-ray structures that match emission features in other wave bands proves the efficacy of the technique. This will be explored in more detail in a future paper (T. DeLaney et al. 2004, in preparation).

Using both extracted spectra and spectral tomography, 80% of the 261 knots were classified into one of the four spectral classes. Histograms showing the radial expansion rates broken down by spectral class are shown in Figure 3. Also included for completeness are the expansion rates from the 29 forward shock filaments presented in DeLaney & Rudnick (2003). The expansion rate distribution of the knots and filaments is very broad; however, when broken down by spectral class, it is clear that each species has its own characteristic motion. The expansion rate distribution of each class holds for both the tomography and spectrum identified sets independently— proving the robustness of the tomography identifications. The Si- and Fe-dominated ejecta knots have the fastest expansion rates, with a mean value of $0.2 \pm 0.01$ percent $yr^{-1}$. The expansion rate, expressed in percent $yr^{-1}$, is independent of projection effects.

To compare to Doppler measurements, we can project the expansion rates onto the plane of the sky. The Si-dominated knots are at an average radius of $95''$, which converts to a transverse velocity of 3100 km s$^{-1}$ for a distance of 3.4 kpc to Cas A. The Fe-dominated knots lie farther out, on average, at a radius of $120''$, yielding an average transverse velocity of 3900 km s$^{-1}$ for the same expansion rate. The Doppler measurements from *XMM* show that the Fe emission is at a larger radius, on average, than the Si emission and that the average line-of-sight velocities are smaller than the average transverse velocities at approximately 1500 km s$^{-1}$ for the Fe and 1000 km
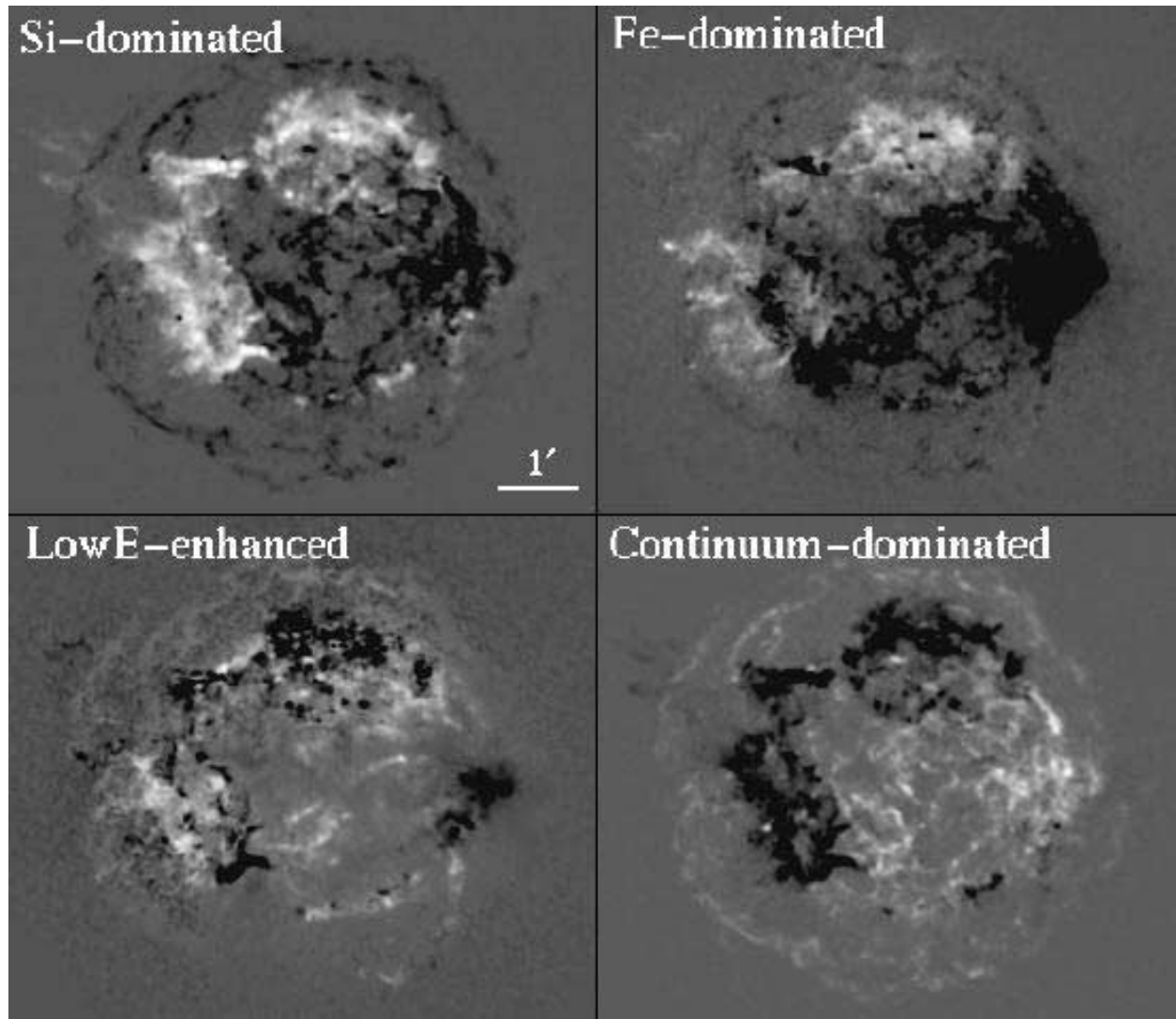
Fig. 2.—Representative tomography images used to spatially identify emission from the four classes whose spectra are shown in Fig. 1. The Si- and Fe-dominated images represent ejecta emission. Note that because of absorption, the ejecta emission on the western side of the remnant is underrepresented. The LowE-enhanced image likely represents clumpy CSM emission analogous to optical QSF emission. The continuum-dominated image possibly represents emission from diffuse CSM swept up by the forward shock.

$s^{-1}$ for the Si (Willingale et al. 2002). The Doppler velocities measured for Si with *Chandra* are slightly faster than those measured with *XMM* at 2000–3000 km s$^{-1}$ (Hwang et al. 2001). The difference between the Doppler measurements for Si could be due to the way in which the zero point in velocity was determined or possibly to the different spectral and spatial resolutions of *XMM* and *Chandra*. The mismatch of Doppler velocities and transverse velocities is not surprising. The average transverse and line-of-sight velocities would only match if the ejecta were uniformly distributed and thus observed at all projected radii such that, on average, projection effects would contribute equally in each case. For Cas A, the ejecta do not appear to be uniformly distributed (Willingale et al. 2002).

The LowE-enhanced knots are moving quite slowly, with a mean expansion rate of 0.05 ± 0.01 percent yr$^{-1}$. The Si- and Fe-dominated knot distribution and the LowE-enhanced knot distribution are narrow with respect to the separation between them, which is consistent with virtually nonoverlapping populations. The continuum-dominated knots and filaments are split into "exterior" and "projected interior," where the

exterior features are the forward shock filaments around the periphery of the remnant. The exterior features have a mean expansion rate of 0.2 ± 0.01 percent yr$^{-1}$, while the expansion rate of the projected interior population varies significantly and includes apparent inward motions. Most of the inward motions are concentrated to the south and west between 170° and 300° azimuth. Radio proper-motion measurements also show inward-moving features in this region (Anderson & Rudnick 1995).

## 3. DISCUSSION

As was found previously with the *Einstein* and *ROSAT* proper-motion measurements (Koralesky et al. 1998; Vink et al. 1998), the X-ray ejecta are moving slower, as a class, relative to the cospatial *population* of optical ejecta and moving faster, as a class, than the cospatial *population* of radio knots (On a case-by-case basis, the small number of matched X-ray/optical and X-ray/radio knots show the same motions; T. DeLaney et al. 2004, in preparation). The X-ray/optical population difference is thought to be due to the density difference between the two
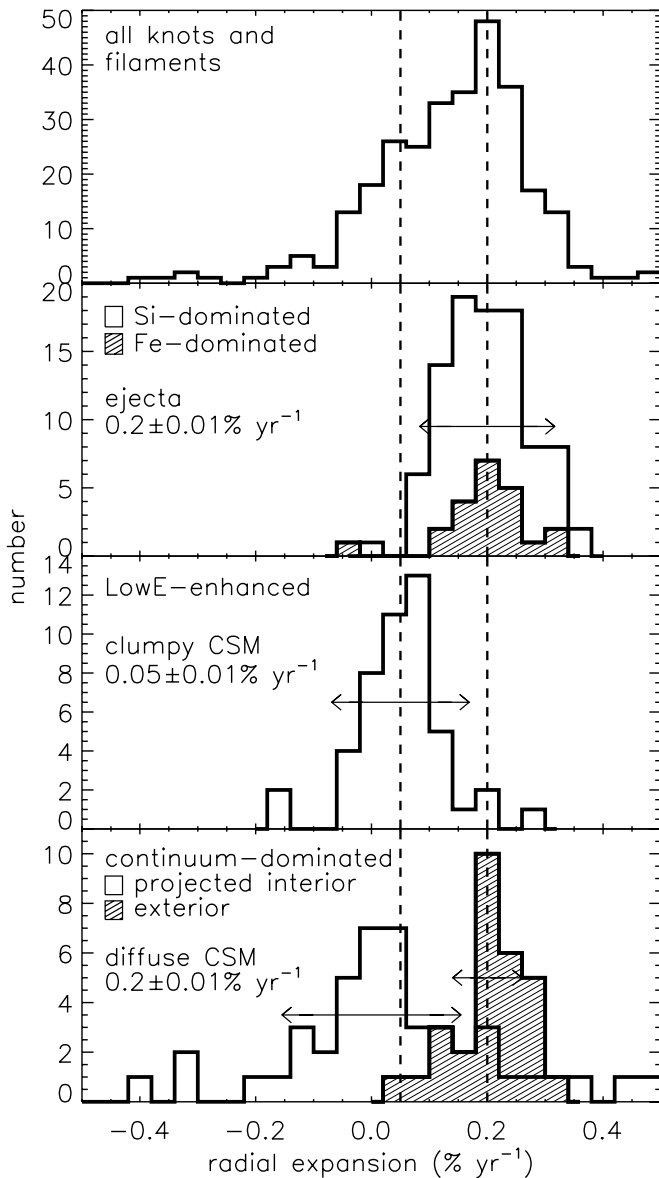
Fig. 3.—Histogram of expansion rates in Cas A. Arrows represent the average measurement error for each population. Dashed lines represent the mean expansion values for the Si-dominated and LowE-enhanced populations. There are also two continuum-dominated knots with expansion rates less than $-0.4\%$ yr$^{-1}$. The exterior continuum-dominated filaments are from DeLaney & Rudnick (2003) and have been included here for completeness. Free expansion corresponds to $0.3\%$ yr$^{-1}$.

populations (Anderson et al. 1994; Hwang et al. 2001; Fesen 2001; DeLaney & Rudnick 2003). High-density ejecta experience very little deceleration, and thus very little disruption, allowing the ejecta to cool rather quickly and emit at optical wavelengths. Low-density ejecta experience more deceleration and are heated to higher temperatures. These ejecta emit at X-ray wavelengths and may even be completely disrupted before they can cool enough to emit optically. The radio emission arises from synchrotron radiation, which requires the amplification of magnetic fields to be strong enough for the emission to be seen. This amplification results from the turbulence associated with ejecta deceleration. If significant deceleration is needed for amplification, radio-emitting knots would be decelerated the most.

Of particular interest is the fact that the Si- and Fe-dominated ejecta have experienced the same fractional deceleration in their expansion rate from the free expansion rate of $0.3\%$ yr$^{-1}$ to $0.2\%$ yr$^{-1}$. The Fe-rich emission (which results from explosive silicon burning near the core of the progenitor) is, on average, exterior to the Si-group emission (which results from explosive oxygen burning farther out from the star's center). This spatial overturning of material could be due to several scenarios: (1) The Si and Fe ejecta may have had different initial velocities imparted from the SN explosion such that the Fe layer overtook the Si layer. (2) The Fe ejecta may have experienced less deceleration at the reverse shock than the Si ejecta (perhaps because of density differences between the two types of ejecta). (3) The overturning may have occurred in the star prior to or during the SN explosion, resulting in a spatial separation between the Fe and Si even in the event of the same initial explosion velocities. These scenarios would not necessarily predict that the Si and Fe would have the same expansion rate, as observed. Furthermore, the X-ray ejecta have the same expansion rate as the forward shock filaments (i.e., homologous expansion, on average), perhaps implying that the two populations are part of a coupled dynamical system in which the pressure in the X-ray ejecta is determined by the forward shock speed, although this does not explain why the optical ejecta would not be affected. Even if initially the different types of ejecta were not coupled    to each other or to the forward shock speed, after interaction with the reverse shock and secondary shocks, the ejecta may now be coupled and expanding with the forward shock (Laming & Hwang 2003).

At the other end of the expansion rate spectrum are the LowE-enhanced knots and filaments. Spatially, many of these features match very well with optical QSF emission, particularly the arc to the south, the emission on the bright ring to the northeast, and much of the interior emission (T. DeLaney et al. 2004, in preparation). On average, QSFs show little or no motion (van den Bergh & Kamper 1985), while the mean expansion rate of the LowE-enhanced knots is $0.05 \pm 0.01$ percent yr$^{-1}$. Based on the spatial and dynamical similarities, we propose that the LowE-enhanced X-ray emission, like the optical QSF emission, represents the clumpy component of the CSM that was deposited by the wind from the progenitor. The slight difference in expansion rates between the optical QSF population and the X-ray LowE-enhanced population might be due to a preexisting density distribution in the progenitor wind (Chevalier & Oishi 2003). On average, less dense X-ray clumps may be accelerated more by the forward shock than more dense optical clumps. The low-energy enhancement in the X-ray spectrum relative to the global X-ray spectrum (i.e., a "softer" X-ray spectrum) is expected as dense clumps are overrun by the forward shock resulting in slow-moving transmitted shocks through the clumps (Chevalier & Oishi 2003), which will produce an X-ray spectrum with a "cooler" characteristic temperature compared to other X-ray components (Hester & Cox 1986; Park et al. 2003).

Another likely CSM component, a diffuse component, was discovered when the "first-light" observation of *Chandra* revealed a thin, continuum-dominated ring of emission around the outer edge of the remnant, which has been identified as the forward shock (Gotthelf et al. 2001). We find similar continuum-dominated knots and filaments across the face of the remnant and propose that these are also forward shock filaments seen in projection. These projected interior filaments are associated with edges and filaments of radio emission (T. DeLaney et al. 2004, in preparation) just as the exterior forward shock filaments are associated with the edge of the radio plateau (Gotthelf et al. 2001). The projected interior and

exterior filaments also have the same X-ray spectral shape (Fig. 1, *bottom panel*), and they are both associated with steep radio spectral index features (Anderson & Rudnick 1996). The projected interior filaments are not evenly distributed across the face of the remnant, but rather are concentrated to the west, where there is significant X-ray absorption (Koehane et al. 1996; Willingale et al. 2002). The "inward" motions and the apparent motions faster than free expansion for the projected filaments are consistent with the forward shock following the path of least resistance through the clumpy medium and showing apparent chaotic behavior when seen face-on. We may also be observing a more complex pattern involving both motions and changes in synchrotron brightness as magnetic fields are amplified in shear layers and in turbulent wakes because of the forward shock wrapping around CSM clumps (Jones & Kang 1993). The interior continuum-dominated filaments have also been interpreted as nonthermal bremsstrahlung emission associated with the ejecta/reverse shock (Bleeker et al. 2001). The *XMM* hard X-ray continuum images show that the continuum-dominated emission in the west is significantly brighter than the exterior forward shock filaments, possibly indicating that the two continuum-dominated populations arise through different emission processes. If the interior filaments are instead internal to the SNR, they are unlikely to arise through X-ray synchrotron emission because the high magnetic field strength will cause rapid aging of electrons at these energies (Vink & Laming 2003).

In summary, the high-resolution proper-motion measurements, along with the spectral classes, reveal that the X-ray emission can be separated into three components, each with a distinct kinematic signature. The ejecta component consists of both Si- and Fe-dominated emission populations, is associated with optical FMK emission, and has been significantly decelerated relative to the FMKs. This greater deceleration of the X-ray ejecta is likely due to the lower densities in this material relative to the optical FMKs. The slow-moving LowE-enhanced emission may be analogous to optical QSF emission, thus representing a clumpy CSM component. A diffuse CSM component may be associated with continuum-dominated emission from material swept up by the forward shock. In this scenario, the chaotic motions of the interior continuum-dominated filaments would be explained as the projected behavior of the forward shock interacting with an inhomogeneous CSM. The exterior continuum-dominated filaments have the same expansion rate as the X-ray ejecta, suggesting a dynamic coupling between the forward shock and the ejecta.

REFERENCES

Agüeros, M. A., & Green, D. A. 1999, MNRAS, 305, 957
Anderson, M., Jones, T. W., Rudnick, L., Tregillis, I. L., & Kang, H. 1994, ApJ, 421, L31
Anderson, M., & Rudnick, L. 1995, ApJ, 441, 307
———. 1996, ApJ, 456, 234
Bleeker, J. A. M., Willingale, R., van der Heyden, K., Dennerl, K., Kaastra, J. S., Aschenbach, B., & Vink, J. 2001, A&A, 365, L225
Chevalier, R., & Oishi, J. 2003, ApJ, 593, L23
DeLaney, T., Koralesky, B., & Rudnick, L. 2002, ApJ, 580, 914
DeLaney, T., & Rudnick, L. 2003, ApJ, 589, 818
Dickel, J. R., Sault, R., Arendt, R. G., Matsui, Y., & Korista, K. T. 1988, ApJ, 330, 254
Fesen, R. A. 2001, ApJS, 133, 161
Gotthelf, E., Koralesky, B., Rudnick, L., Jones, T., Hwang, U., & Petre, R. 2001, ApJ, 552, L39
Hester, J. J., & Cox, D. P. 1986, ApJ, 300, 675
Hughes, J. P. 1999, ApJ, 527, 298
———. 2000, ApJ, 545, L53
Hughes, J. P., Rakowski, C. E., Burrows, D. N., & Slane, P. O. 2000, ApJ, 528, L109
Hwang, U., Holt, S., & Petre, R. 2000, ApJ, 537, L119

Hwang, U., & Laming, J. M. 2003, ApJ, 597, 362
Hwang, U., Szymkowiak, A. E., Petre, R., & Holt, S. S. 2001, ApJ, 560, L175
Jones, T. W., & Kang, H. 1993, ApJ, 402, 560
Kamper, K., & van den Bergh, S. 1976, ApJS, 32, 351
Katz-Stone, D. M., & Rudnick, L. 1997, ApJ, 488, 146
Koehane, J. W., Rudnick, L., & Anderson, M. C. 1996, ApJ, 466, 309
Koralesky, B., Rudnick, L., Gotthelf, E., & Keohane, J. 1998, ApJ, 505, L27
Laming, J. M., & Hwang, U. 2003, ApJ, 597, 347
Lawrence, J. L., MacAlpine, G. M., Uomoto, A., Woodgate, B. E., Brown, L. W., Oliversen, R. J., Lowenthal, J. D., & Liu, C. 1995, AJ, 109, 2635
Park, S., Burrows, D. N., Garmire, G. P., Nousek, J. A., Hughes, J. P., & Williams, R. M. 2003, ApJ, 586, 210
Reed, J. E., Hester, J. J., Fabian, A. C., & Winkler, P. F. 1995, ApJ, 440, 706
Thorstensen, J., Fesen, R., & van den Bergh, S. 2001, AJ, 122, 297
Tuffs, R. 1986, MNRAS, 219, 13
van den Bergh, S., & Kamper, K. 1985, ApJ, 293, 537
Vink, J., Bloemen, H., Kaastra, J. S., & Bleeker, J. A. M. 1998, A&A, 339, 201
Vink, J., & Laming, J. M. 2003, ApJ, 584, 758
Willingale, R., Bleeker, J. A. M., van der Heyden, K. J., Kaastra, J. S., & Vink, J. 2002, A&A, 381, 1039